Valley-resolved interband excitation and emission in gapped graphene

Hubin Cui,[1] Liang Li [1,*] Tengfei Huang,[1] Jiapeng Li,[1] Pengfei Lan,[1,†] and Peixiang Lu [1,2]

[1]*School of Physics and Wuhan National Laboratory for Optoelectronics,*
Huazhong University of Science and Technology, Wuhan 430074, China
[2]*Hubei Key Laboratory of Optical Information and Pattern Recognition, Wuhan Institute of Technology, Wuhan 430205, China*

We theoretically investigate the electronic dynamics in gapped graphene driven by a bicircular field. The results indicate that the residual population on the conduction band is obviously asymmetric in the K and K′ valleys. Through analyzing the electron trajectory, we find that the interband transitions are determined by the compensation of two phases: the dynamic phase and the full dipole phase (including the transition dipole phase and the Berry phase). When the rates of change of the dynamic phase and the full dipole phase nearby the ionization time have the inverse signs, the unidirectional interband transition from the valence band (VB) to the conduction band (CB) results in the constructive interference of the population. In contrast, when they have the same signs, the bidirectional transition (CB→VB and VB→CB) results in the destructive interference. The constructive interference and the destructive interference lead to the asymmetric distribution of the CB population. Moreover, we also investigate the harmonic emission and find that only the $3n + 2$ harmonics are generated in the cutoff region. This phenomenon can be attributed to the asymmetric distribution of the CB population and the trefoil vector potential of the electric field. Due to the dependence on population distribution, the harmonics can be a promising optical way to detect the valley excitation of the gapped graphene.

I. INTRODUCTION

Interaction between ultrafast intense optical pulse and solids has opened up a platform to study electronic dynamics in solids. Many fascinating phenomena have been observed and investigated, such as high-order harmonic generation (HHG) [1–5] and light-field-driven current [6–10]. Underlying electronic dynamics has been investigated in the context of strong-field physics. Two mechanisms were proposed to understand these phenomena: intraband and interband dynamics.

In the strong-field regime, electrons in solids follow the reciprocal space trajectory determined by the vector potential of the laser field. When electrons are driven to the regimes nearby the minimum band gap between the conduction band (CB) and the valence band (VB), its wave function can be coherently split: one part of the wave function can experience an interband transition, whereas the other part remains in its initial band (intraband motion). This dynamical process is described by the Landau-Zener (LZ) transition [11,12]. The insight of the electronic dynamics has provided a good understanding of the CB population distribution and related physical phenomena [7–10,13–17]. For instance, the interference fringes of the CB population in graphene exposed to a suboptical-cycle light are due to a series of coherent interband transitions [7,14–16], which is well-known as Landau-Zener-Stückelberg (LZS) interference [12]. Moreover, the residual current induced by linearly polarized driving pulses in monolayer graphene is sensitive to the electric-field wave form. This current is due to an asymmetric CB population, and its dependence on the wave form is related to the LZS interference [7,9].

The interference of the LZ transitions is determined by the propagation phases accumulated along the quantum pathway in reciprocal space. In a symmetric system, the propagation phase only includes the dynamical phase. But for a system with broken symmetry, the full dipole phase is non-negligible and plays a significant role on the interband dynamics during the evolution of electrons. Although many previous works have studied the role of the full dipole phase in HHG phenomena [18–22], its role in the underlying dynamical process is rarely of concern. Here, based on trajectory analysis, we provide a method to analyze how the full dipole phases affect the interband transition of electrons and lead to an asymmetric excitation. In such a method, we can consider the electronic trajectory and the propagation phases simultaneously, which makes it an obvious choice to analyze the behaviors of electrons during the whole light-driven process.

We consider the electronic dynamics in gapped graphene, which is a well-known two-dimensional material with nonzero Berry curvature. Graphene is also an excellent platform with which to study electronic dynamics driven by an ultrafast strong field, because of its broadband and ultrafast optical response, weak screening, and high damage threshold [23,24]. Recently, HHG has been demonstrated as a promising tool to probe the electronic structure and the ultrafast dynamics [25–29]. Here, we investigate the properties of harmonic
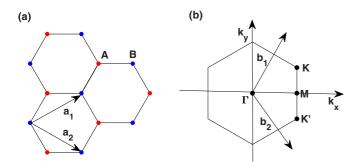
FIG. 1. (a) The honeycomb lattice of graphene with two sublattices, A and B. (b) The first Brillouin zone of graphene with two nonequivalent valleys, K and K'.

emission contributed by two nonequivalent valleys in gapped graphene.

II. THEORETICAL MODEL

Graphene has a honeycomb crystal structure made of two sublattices [23], A and B shown in Fig. 1(a), and its first Brillouin zone contains two nonequivalent Dirac points K and K' [Fig. 1(b)], corresponding to two valleys in energy dispersion. Pristine graphene is a zero-band-gap material due to its symmetries. The inversion symmetry can be broken by changing the external environment like positioning on an incommensurate substrate [30,31], and a band gap is opened correspondingly.

In gapped graphene, the electronic dynamics driven by an untrafast strong field is described as the time-dependent Schrödinger equation (TDSE):

$$i\hbar \frac{d\Psi}{dt} = \hat{H}(t)\Psi, \quad (1)$$

where $\hat{H}(t) = \hat{H}_0 - e\mathbf{F}(t) \cdot \mathbf{r}$ is the Hamiltonian in length gauge with an applied field $\mathbf{F}(t)$, and $\hat{H}_0$ is the intrinsic Hamiltonian of the gapped graphene. The second term represents the interaction of the laser with the graphene. Atomic units are used in this article unless otherwise stated. In a tight-binding model, $\hat{H}_0$ has the following form [32]:

$$H_0 = \begin{bmatrix} \Delta/2 & \gamma f(\mathbf{k}) \\ \gamma f^*(\mathbf{k}) & \Delta/2 \end{bmatrix}. \quad (2)$$

Here, Δ is the band gap between the CB and the VB, $\gamma = -3.03$ eV is the hopping integral, and $f(\mathbf{k})$ is given by

$$f(\mathbf{k}) = \exp\left(i\frac{ak_x}{\sqrt{3}}\right) + 2\exp\left(-i\frac{ak_x}{2\sqrt{3}}\right)\cos\left(\frac{ak_y}{2}\right), \quad (3)$$

where $a = 2.46$ Å is the lattice constant. The energies of the CB and the VB are obtained from $\hat{H}_0$:

$$E_c = +\sqrt{\gamma^2|f(\mathbf{k})|^2 + \frac{\Delta^2}{4}},$$

$$E_v = -\sqrt{\gamma^2|f(\mathbf{k})|^2 + \frac{\Delta^2}{4}}. \quad (4)$$

When an electric field is applied, electrons undergo both the intraband motion and the interband transition. The intraband motion follows the Bloch acceleration theorem [33],

$\mathbf{k}(t) = \mathbf{k}_0 + \frac{e}{\hbar}\int_{-\infty}^{t} \mathbf{F}(t)dt$, with initial momentum $\mathbf{k}_0$, which determines the trajectories of electrons in reciprocal space. The corresponding adiabatic wave functions are well-known Houston functions [34]:

$$\Phi_m^{(H)}(r,t) = \Psi_{\mathbf{k}(t)}^{(m)}(r)\exp\left[i\phi_m^{(D)}(\mathbf{k}(t)) + i\phi_m^{(B)}(\mathbf{k}(t))\right], \quad (5)$$

where $m = c$ and v is the band index of the CB and the VB. $\Psi_{\mathbf{k}(t)}^{(m)}(r)$ are the Bloch-band eigenfunctions in the absence of the pulse field. $\phi_m^{(D)}(\mathbf{k}(t))$ and $\phi_m^{(B)}(\mathbf{k}(t))$ represent the dynamic phase and the Berry phase [35,36], respectively, and their expressions are as follows:

$$\phi_m^{(D)} = -\frac{1}{\hbar}\int_{-\infty}^{t} E_m(\mathbf{k}(t'))dt',$$

$$\phi_m^{(B)} = \frac{e}{\hbar}\int_{-\infty}^{t} \mathbf{F}(t') \cdot \mathbf{d}_{mm}(\mathbf{k}(t'))dt'. \quad (6)$$

Here, $\mathbf{d}_{mm} = \langle\Psi_{\mathbf{k}}^m|i\frac{\partial}{\partial\mathbf{k}}|\Psi_{\mathbf{k}}^m\rangle$ is the Berry connection for band m. The wave function can be expanded in the Houston functions:

$$\Psi_{\mathbf{k}_0}(r,t) = \sum_{m=c,v} a_{m\mathbf{k}_0}(t)\Phi_{mk_0}^{(H)}(r,t) \quad (7)$$

By solving the TDSE, one can derive the two level density matrix equations [3,4,10] as follows:

$$\dot{\Pi}(\mathbf{k}(t)) = -\frac{\Pi(\mathbf{k}(t))}{T_2} + i\Omega^*(\mathbf{k}(t))w(\mathbf{k}(t))e^{iS(\mathbf{k}(t))},$$

$$\dot{n}_m(\mathbf{k}(t)) = is_m\Omega(\mathbf{k}(t))\Pi(\mathbf{k}(t))e^{-iS(\mathbf{k}(t))} + \text{c.c.}, \quad (8)$$

where n_m is the population of the valence band ($m = v$) and the conduction ($m = c$) band, Π is the off-diagonal element of the density matrix, and $w = n_v - n_c$ is the population difference. $s_m = 1$ and -1 for $m = v$ and c, respectively. $\Omega = \mathbf{F} \cdot \mathbf{d}_{cv}$ is the Rabi frequency, $\mathbf{d}_{cv} = \langle\Psi_{\mathbf{k}}^c|i\frac{\partial}{\partial\mathbf{k}}|\Psi_{\mathbf{k}}^v\rangle$ is the transition dipole [37–39], and $S = \phi_c^{(D)}(\mathbf{k}(t)) - \phi_v^{(D)}(\mathbf{k}(t)) + \phi_c^{(B)}(\mathbf{k}(t)) - \phi_v^{(B)}(\mathbf{k}(t))$ is the accumulated phase during the nonadiabatic evolution in k space. T_2 is the dephasing time in graphene, and 5 fs is used in our simulations [40–45].

Equations (8) describe the interband dynamics between the CB and the VB and can be solved numerically. Apparently, Ω and S determine the interband transition together; we define their product as the ionization rate [3,4]: $\chi = \Omega e^{-iS} = |\Omega|e^{iS'}$, with $S' = \phi^D + \phi^T + \phi^B$, where $\phi^T = \arg\{\mathbf{F} \cdot \mathbf{d}_{cv}\}$ is the transition dipole phase (TDP) extracted from Ω, and ϕ^D and ϕ^B are the dynamic phase and the Berry phase (BP), respectively. Note that both the TDP and the BP are not gauge-invariant individually. Hence, we focus on their joint role and refer to their summation as the full dipole phase in this article, i.e., $\phi^F = \phi^B + \phi^T$. It can be demonstrated that the rate of change of the summation is a gauge-invariant quantity following Ref. [46], i.e., $\nabla_t\phi^F = \mathbf{F} \cdot (\mathbf{d}_{cc} - \mathbf{d}_{vv}) - \mathbf{F} \cdot \nabla_{\mathbf{k}}\phi^T$. It should be noted that the joint full dipole phase stems from the broken inversion symmetry of gapped graphene. In this article, we adopt a common gauge in the tight-binding description of gapped graphene to show its effect on the interband transition.

According to the LZS interference [12], in a periodic electric field, electrons repeatedly traverse the transition zone nearby the minimum band-gap, where a series of transition

events happen. The interference of these transition events leads to the residual CB population.

We also calculate the interband current and the interband harmonic emission, and the harmonic spectrum is obtained from the Fourier transform of the current. Their expressions are as follows:

$$\mathbf{J}_{er}(t) = \frac{d}{dt}\left[\sum_{\mathbf{k}_0 \in BZ} \Pi_{\mathbf{k}_0} \mathbf{p}_{cv}(\mathbf{k}(t)) + \text{c.c.}\right],$$

$$H_{er}(\omega) = |FT\{\mathbf{J}_{er}(t)\}|^2, \tag{9}$$

Here, $\mathbf{p}_{cv}(k)$ is the momentum matrix element between the CB and the VB, calculated by $\mathbf{p}_{cv}(\mathbf{k}) = \langle c, \mathbf{k}|\nabla_{\mathbf{k}} H|v, \mathbf{k}\rangle$.

III. RESULTS AND DISCUSSION

In our simulations, a multicycle bicircular field composed of a fundamental-frequency light and a frequency-doubling light is applied. The vector potential is given by

$$\mathbf{A} = \frac{E_0 f(t)}{\sqrt{2}\omega}\left\{\left[\cos(\omega t) + \frac{1}{2}\cos(2\omega t + \varphi)\right]\vec{\mathbf{e}}_x\right.$$

$$\left. + \left[\sin(\omega t) - \frac{1}{2}\sin(2\omega t + \varphi)\right]\vec{\mathbf{e}}_y\right\}, \tag{10}$$

where E_0 is the peak electric field strength, and $f(t)$ is the temporal envelope with a sine squared shape. φ is the relative phase, and the orientation of the trefoil vector potential is adjustable by changing φ. The calculation is performed with the following laser pulse parameters: the peak intensity of the laser is $I_0 = 0.8\ \text{TW/cm}^2$, the wavelength of the fundamental-frequency light is 3.5 μm, the duration is set as ten optical cycles of the fundamental-frequency light, and the relative phase is $\varphi = -\pi/2$.

Figure 2 shows the normalized CB population after excitation. For the pristine graphene [0 eV, Fig. 2(a)], the distribution of the CB population in the K and K' valleys is almost same. For the small-gap graphene [1 and 2 eV, Figs. 2(b) and 2(c)], the asymmetric population appears, and the asymmetry is enhanced with an increase of the band gap. When the band gap is 3 eV [Fig. 2(d)], the asymmetry peaks with the CB population occurring in the opposite zones of two valleys. For the K' valley, the population occurs inside the black boundary [Fig. 2(d)]; but for the K valley, the population occurs outside the black boundary. Besides, it is worth noting that the population in the K and K' valleys depends on both the helicity and the orientation of the vector potential.

To understand the mechanism of this phenomenon intuitively, we draw a schematic diagram shown in Fig. 3. The formation of the CB population depends on the interference of the electron trajectories. For clarity, we choose the electron trajectories with initial momenta at A1, A2, B1, and B2 [shown in Fig. 3(a)]. A1 and B2 represent the regions with nonzero CB population, and A2 and B1 stand for the regions with vanishingly small CB population. We have confirmed that other points in each region have similar dynamical properties.

In Figs. 3(b) and 3(c), we show the TDP and the difference of the Berry curvature between the VB and the CB,
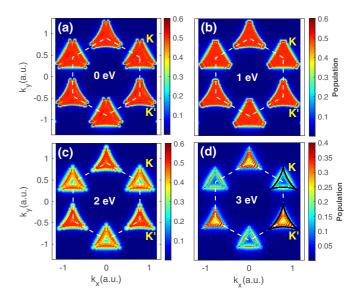

FIG. 2. The normalized CB population after excitation with different band gaps: 0 eV (a), 1 eV (b), 2 eV (c), and 3 eV (d). The white dashed line shows the boundary of the first Brillouin zone with the K and K' points indicated. The black solid lines in panel (d) show the boundary of the population.

respectively. One can see that the TDP and the BP are on the left-hand side and the right-hand side around the K' point, respectively, and opposite around the K point. Note that their relative magnitudes during the evolution depend on the parameters of the electric field. Here we assume the magnitude of the TDP is larger than that of the BP, and thus a residual
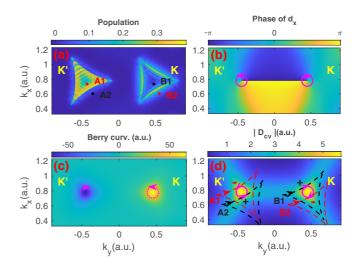

FIG. 3. (a) The residual CB population in the K and K' valleys. A1, A2, B1, and B2 are initial points in k space selected for the corresponding regions. (b) The phase of the x component of transition dipole elements $\mathbf{d}_{cv}$. Arrows show the helicity of the phase. The phase of d_y has the same helicity. (c) Difference of the Berry curvature between the VB and the CB. According to the Stokes theorem, the inverse helicity of the Berry phase around the K and K' points is deduced (shown with arrows). (d) The transition dipole amplitude and the trajectories of A1, A2, B1, and B2 shown as the red or black dashed lines.
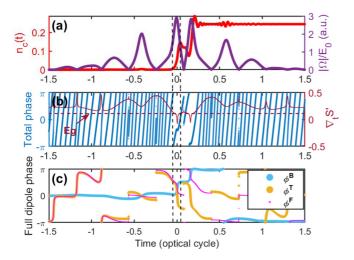
FIG. 4. (a) The CB population (red line) and the modules of Ω (purple line) normalized by the peak field strength along the electron trajectory of A1 and B2. (b) Total phase S' (blue line) and $\nabla_t S'$ (solid red line) with the minimum band gap indicated with a horizontal dashed red line. (c) Full dipole phase including the TDP and the BP.
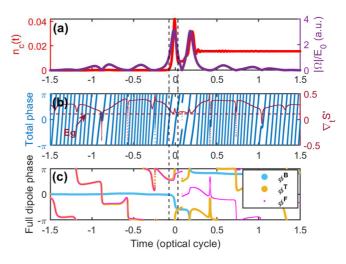

FIG. 5. (a) The CB population (red line) and the modules of Ω (purple line) normalized by the peak field strength along the electron trajectory of A2 and B1. (b) Total phase S' (blue line) and $\nabla_t S'$ (solid red line) with the minimum band gap indicated with a horizontal dashed red line. (c) Full dipole phase including the TDP and the BP.

full dipole phase is expected to have the same helicity as the TDP as shown in Fig. 3(d).

Note that the transition from π to $-\pi$ is smooth. The extracted TDP (ϕ^T) has the same helicity compared to the phase of d_{cv} nearby the K and K′ points, which can be deduced from a derivation of Ω or a numerical verification. In Fig. 3(d), the electron trajectories for A1, A2, B1, and B2 are shown with the red or black dashed lines. When electrons with initial momenta A1 and B2 traverse the transition zone near the minimum band gap, the full dipole phase decreases (marked as red sign "−"). On the contrary, when electrons with initial momenta A2 and B1 traverse the transition zone, the full dipole phase increases (marked as black sign "+").

As mentioned above, the interband transition can be described by $\chi = |\Omega| e^{i(\phi^T + \phi^D + \phi^B)}$. In the following, we show how one can analyze the interband transition with the interference of the electron trajectories.

Figure 4 describes the trajectories of electrons initially located at A1 and B2. In Fig. 4(a), the red line shows the time-dependent CB population, and the purple line shows the modules of Ω normalized with the peak field strength E_0. We can see that the transition events occur only when $|\Omega| = |\mathbf{F} \cdot \mathbf{d}_{cv}|$ is maximum. For convenience, one of the transition events is chosen and marked with the vertical dashed black lines. In Figs. 4(b) and 4(c), the time-dependent total phase and the full dipole phase are displayed respectively. Note that the dynamic phase always increases because of a positive band gap. During the transition event, we can see that the total phase [blue line in Fig. 4(b)] shows a nonmonotonic behavior: almost static near the peak of $|\Omega|$. For clarity, $\nabla_t S' = E_c - E_v + F \cdot (d_{cc} - d_{vv}) + \nabla_t \phi^T$ (solid red line) is calculated to describe the behavior of the total phase.

We can see that $\nabla_t S' < E_g$ (minimum band gap) and close to zero at the ionization time. It is due to the decreasing full dipole phase ($\nabla_t \phi^F < 0$) as clearly seen in Fig. 4(c). In Fig. 4(c), the TDP (yellow line) and the BP (blue line) are plotted separately to show their individual contributions to

the full dipole phase in the present gauge we adopted. As a composition, the full dipole phase (pink line) has a negative rate of change. Within the transition, the full dipole phase changes: $\Delta \phi^F \approx -\pi/2$. Due to the compensation of the dynamic phase and the full dipole phase, the total phase only changes: $\Delta \phi^D + \Delta \phi^F \approx \pi$. Apparently, the slowly varying total phase leads to the unidirectional transition (VB→CB, or CB→VB) and the accumulation of the CB population (constructive interference).

A similar analysis is performed for A2 and B1. Figure 5 describes the trajectories of electrons initially located at A2 and B1. Differently, the total phase is monotonic during the transition, and $\nabla_t S' > E_g$. This is due to the increasing full dipole phase ($\nabla_t \phi^F > 0$) [Fig. 5(c)]. Within the transition, the full dipole phase changes $\Delta \phi^F \approx \pi/2$, and hence the total phase changes a lot: $\Delta \phi^D + \Delta \phi^F \approx 2\pi$. The rapidly varying total phase leads to the switch between the increase and the decrease of the CB population (bidirectional transition: VB→CB and CB→VB) and a small residual CB population (destructive interference).

From the discussion above, we can see that the role of the full dipole phase in the interband transition is significant when the rate of change of the full dipole phase is comparable to the rate of change of the dynamical phase at the ionization time. To figure out how the TDP and the BP act on the interband transition as a whole, we furthermore calculate the same situation but discard the full dipole phase manually. Note that the results of discarding one of the TDP or the BP are only valid for the certain gauge adopted in this paper due to their individual dependence on a gauge choice. In Fig. 6(a), when both the TDP and the BP are discarded, the residual CB population is small and similar in K and K′ valleys. In Figs. 6(b) and 6(c), either the TDP or the BP is discarded, both the K and K′ valleys are excited strongly, and the opposite CB population appears for these two cases. In Fig. 6(d), when both of them are included, the population distribution is similar to that in Fig. 6(b), but the population is smaller.
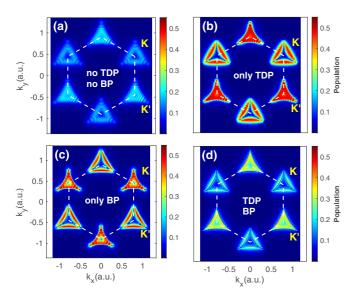
FIG. 6. The residual CB population under the situations: (a) Both the TDP and the BP are discarded. (b) Only BP is discarded. (c) Only the TDP is discarded. (d) Both the TDP and the BP are included.

In Fig. 7, part of the dynamical process of A1 and B2 under the four situations of Fig. 6 is shown. The dashed line marks the time t_p of the peak of $|\Omega|$. When one of the TDP or the BP is included (blue and green lines), the total phases are quite different near t_p, and the amplitude of the transition with only the TDP is much larger than the case with only the BP. When both of them are included (red line), the total phase is almost stationary near t_p. Correspondingly, the amplitude of the transition is smaller than that of the case with only the TDP, which can explain the smaller CB population in Fig. 6(d). These results indicate that a negative or positive rate of change of the full dipole phase plays an opposite role in the interband transition for a certain initial point.

Next we show how the asymmetric excitation of the two valleys affects the harmonic emission. Following Eqs. (9),
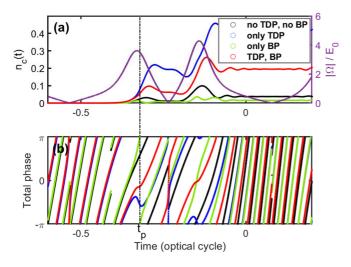

FIG. 7. (a) The time-dependent CB population of A1 and B2 under the different situations, the same as those in Fig. 6. (b) The corresponding total phase.
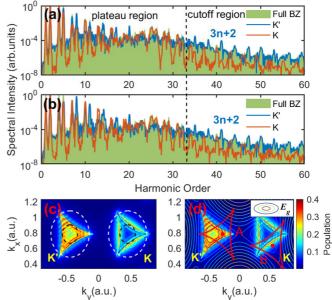

FIG. 8. (a) The harmonic spectra obtained from the different zones: the full Brillouin zone (green area), the K′ valley (blue line), and the K valley (orange line). (b) The harmonic spectra obtained from the selected zones shown in panel (c): the full Brillouin zone (green area), the outside zone of the K′ valley (blue line), and the outside zone of the K valley (orange line). (c) The selected zones between two concentric circles (i.e., inner black circles and outer white circles) in the K and K′ valleys. (d) A schematic diagram for harmonic emission. The contour lines describe the k-dependent band gap: $E_g = E_c - E_v$. The red lines represent the trajectories of the corresponding initial points (red points).

we obtain the interband current and the HHG spectra. In Fig. 8(a), one can see two regions in the total HHG spectra: the plateau region (<33 harmonics) and the cutoff region (about 33–60 harmonics). The former has both the $3n + 1$ and $3n + 2$ harmonics, but the latter has only the $3n + 2$ harmonics. It is an interesting phenomenon that has not been discussed before. To understand the underlying reason, we separate the total harmonic spectrum into the contributions from the K′ (blue line) and K (orange line) valleys. Apparently, for the plateau region, the K and K′ valleys contribute to the $3n + 1$ and $3n + 2$ harmonics, respectively [47–50]. However, for the cutoff region, only the K′ valley contributes to the $3n + 2$ harmonics. Furthermore, in Fig. 8(b), we calculate the HHG spectra contributed by the different zones of the K and K′ valleys. We can see that the outside zone [seen in Fig. 8(c), the zone between the two concentric circles] of the K′ valley contributes to the $3n + 2$ harmonics in the cutoff region. However, the outside zone of the K valley only contributes to the low-order harmonics in the plateau region.

To understand these results, we draw a schematic diagram in Fig. 8(d), the contour lines describe the k-dependent band gap: $E_g = E_c - E_v$, the red lines represent the trajectories of the corresponding initial points (red points A and B) in the outside zones. We can see that the trajectory of A passes the Brillouin zone with a large band gap, but the trajectory of B passes the Brillouin zone with a small band gap.
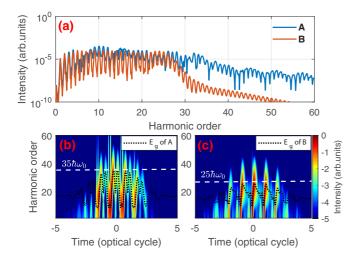
FIG. 9. (a) The harmonic spectra obtained from the single point A (blue line) and the single point B (orange line). (b) The black dashed line shows the time-dependent band gap along the trajectory of point A, and the maximum band gap is marked with a white dashed line. The time-frequency spectrogram (color map) is for point A. The maximum values are normalized to 1 for clarity. A logarithmic color scale is used. (c) The same as panel (b), but for point B.

In Fig. 9(a), we show the harmonics contributed by the single point A (blue line) and the single point B (orange line), respectively, and all the harmonics exist for a single point. Point A has a higher cutoff ($\sim$H35) than point B ($\sim$H25). In Figs. 9(b) and 9(c), the time-dependent band gap $E_g(t) = E_c(\mathbf{k}(t)) - E_v(\mathbf{k}(t))$ and the time-frequency spectrogram are shown for points A and B, respectively. As we know in the three-step model [3], the electron-hole pair emits a photon ω with energy equal to the that of the band gap at the momentum of recombination. Along the electronic trajectories, the maximum band gaps of points A and B are $35\hbar\omega_0$ and $25\hbar\omega_0$, respectively, which is consistent with the maximum harmonic energy in the time-frequency spectrogram, i.e., the cutoff.

As mentioned above, most of the electrons in the K' valley have a cutoff energy higher than that in the K valley. Therefore, the trajectories' interference of the electrons in K' valley leads to the $3n + 2$ harmonics with a higher cutoff, whereas the electrons in the K valley contribute to the $3n + 1$ harmonics with a lower cutoff. As a result of the superposition of the $3n + 1$ and $3n + 2$ harmonics, only the $3n + 2$ harmonics are left in the cutoff region. Clearly, it is the nonequivalent band structure of two valleys and the trefoil vector potential that lead to the difference of the harmonic emission of the two valleys together.

We also calculate the HHG spectra with different orientations of the trefoil vector by changing the relative phase of the bicircular field in Fig. 10. Note that a change of 2π in the relative phase corresponds to a 120° rotation in the orientation of the electric field. It can be seen that the intensity of the $3n + 1$ and $3n + 2$ harmonics in the cutoff region depends on the orientation of the trefoil vector. Clearly, the orientation of the trefoil vector determines the maximal emission energy of
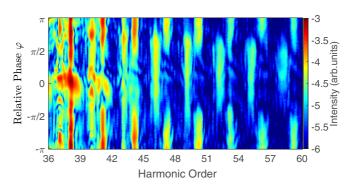

FIG. 10. The relative-phase-resolved intensity of the harmonics in the cutoff region. A logarithmic color scale is used.

electrons in the two valleys by modulating the electronic trajectories. Due to the dependence of electronic excitation and emission on the electronic trajectories, both the CB population and the interband emission are dependent on the orientation of the trefoil vector. It can be a promising way to control the electronic excitation in the CB and detect its distribution with the HHG spectra.

IV. CONCLUSION

We theoretically investigate the electronic dynamics in gapped graphene driven by a bicircular field and analyze the formation of the asymmetric CB population in the K and K' valleys. Through analyzing the electron trajectory, we demonstrate the important role of the full dipole phase on the interband transition. The full dipole phase and the dynamic phase determine the transitions in a coupled manner: when their rate of change have the opposite signs, a slowly varying total phase leads to the constructive interference of the population. In contrast, when their rates of change have the same signs, a rapidly varying total phase leads to the destructive interference of the population. We also investigate the harmonic emission in gapped graphene, we find that only the $3n + 2$ harmonics are generated in the cutoff region. This phenomenon is due to the asymmetric distribution of the CB population in the K and K' valleys and the trefoil vector of the bicircular field. Further calculations indicate that the CB population distribution and the intensity of the $3n + 1$ and $3n + 2$ harmonics in the cutoff region depend on the orientation of the trefoil vector. Due to the dependence, the harmonics can be a promising optical way to detect the CB population distribution in gapped graphene.

ACKNOWLEDGMENTS

[1] S. Ghimire, A. D. DiChiara, E. Sistrunk, P. Agostini, L. F. DiMauro, and D. A. Reis, Nat. Phys. **7**, 138 (2011).

[2] T. T. Luu, M. Garg, S. Y. Kruchinin, A. Moulet, M. T. Hassan, and E. Goulielmakis, Nature (London) **521**, 498 (2015).

[3] G. Vampa, C. R. McDonald, G. Orlando, D. D. Klug, P. B. Corkum, and T. Brabec, Phys. Rev. Lett. **113**, 073901 (2014).

[4] L. Li, P. Lan, X. Zhu, T. Huang, Q. Zhang, M. Lein, and P. Lu, Phys. Rev. Lett. **122**, 193901 (2019).

[5] L. Li, P. Lan, X. Zhu, and P. Lu, Phys. Rev. Lett. **127**, 223201 (2021).

[6] A. Schiffrin, T. Paasch-Colberg, N. Karpowicz, V. Apalkov, D. Gerster, S. Mühlbrandt, M. Korbman, J. Reichert, M. Schultze, S. Holzner *et al.*, Nature (London) **493**, 70 (2013).

[7] T. Higuchi, C. Heide, K. Ullmann, H. B. Weber, and P. Hommelhoff, Nature (London) **550**, 224 (2017).

[8] L. Costa, M. Betz, M. Spasenović, A. D. Bristow, and H. M. Van Driel, Nat. Phys. **3**, 632 (2007).

[9] C. Heide, T. Higuchi, H. B. Weber, and P. Hommelhoff, Phys. Rev. Lett. **121**, 207401 (2018).

[10] Y. Zhang, J. Li, L. Li, T. Huang, X. Zhu, P. Lan, and P. Lu, Opt. Express **29**, 17387 (2021).

[11] C. Zener, Proc. R. Soc. Lond. A **137**, 696 (1932).

[12] S. N. Shevchenko, S. Ashhab, and F. Nori, Phys. Rep. **492**, 1 (2010).

[13] S. A. Oliaei Motlagh, F. Nematollahi, V. Apalkov, and M. I. Stockman, Phys. Rev. B **100**, 115431 (2019).

[14] S. Y. Kruchinin, M. Korbman, and V. S. Yakovlev, Phys. Rev. B **87**, 115201 (2013).

[15] T. Paasch-Colberg, S. Y. Kruchinin, Ö. Sağlam, S. Kapser, S. Cabrini, S. Muehlbrandt, J. Reichert, J. V. Barth, R. Ernstorfer, R. Kienberger *et al.*, Optica **3**, 1358 (2016).

[16] H. K. Kelardeh, V. Apalkov, and M. I. Stockman, Phys. Rev. B **91**, 045439 (2015).

[17] C. Lefebvre, D. Gagnon, F. Fillion-Gourdeau, and S. MacLean, J. Opt. Soc. Am. B **35**, 958 (2018).

[18] R. Silva, Á. Jiménez-Galán, B. Amorim, O. Smirnova, and M. Ivanov, Nat. Photonics **13**, 849 (2019).

[19] T. T. Luu and H. J. Wörner, Nat. Commun. **9**, 916 (2018).

[20] Á. Jiménez-Galán, R. Silva, O. Smirnova, and M. Ivanov, Nat. Photonics **14**, 728 (2020).

[21] A. Chacón, D. Kim, W. Zhu, S. P. Kelly, A. Dauphin, E. Pisanty, A. S. Maxwell, A. Picón, M. F. Ciappina, D. E. Kim *et al.*, Phys. Rev. B **102**, 134115 (2020).

[22] T. Nag, R.-J. Slager, T. Higuchi, and T. Oka, Phys. Rev. B **100**, 134301 (2019).

[23] A. H. Castro Neto, F. Guinea, N. M. R. Peres, K. S. Novoselov, and A. K. Geim, Rev. Mod. Phys. **81**, 109 (2009).

[24] F. J. Garcia de Abajo, ACS Photonics **1**, 135 (2014).

[25] G. Vampa, T. Hammond, N. Thiré, B. Schmidt, F. Légaré, C. McDonald, T. Brabec, and P. Corkum, Nature (London) **522**, 462 (2015).

[26] G. Vampa, C. R. McDonald, G. Orlando, P. B. Corkum, and T. Brabec, Phys. Rev. B **91**, 064302 (2015).

[27] M. Schultze, K. Ramasesha, C. Pemmaraju, S. Sato, D. Whitmore, A. Gandman, J. S. Prell, L. Borja, D. Prendergast, K. Yabana *et al.*, Science **346**, 1348 (2014).

[28] N. Yoshikawa, T. Tamaya, and K. Tanaka, Science **356**, 736 (2017).

[29] L. Li, T. Huang, P. Lan, J. Li, Y. Zhang, X. Zhu, L. He, W. Cao, and P. Lu, Phys. Rev. Lett. **128**, 027401 (2022).

[30] M. S. Nevius, M. Conrad, F. Wang, A. Celis, M. N. Nair, A. Taleb-Ibrahimi, A. Tejeda, and E. H. Conrad, Phys. Rev. Lett. **115**, 136802 (2015).

[31] D. Jariwala, A. Srivastava, and P. M. Ajayan, J. Nanosci. Nanotechnol. **11**, 6621 (2011).

[32] T. G. Pedersen, A.-P. Jauho, and K. Pedersen, Phys. Rev. B **79**, 113406 (2009).

[33] F. Bloch, Z. Phys. **52**, 555 (1929).

[34] W. Houston, Phys. Rev. **57**, 184 (1940).

[35] M. V. Berry, Proc. R. Soc. London, Ser. A **392**, 45 (1984).

[36] D. Xiao, M.-C. Chang, and Q. Niu, Rev. Mod. Phys. **82**, 1959 (2010).

[37] F. Wilczek and A. Zee, Phys. Rev. Lett. **52**, 2111 (1984).

[38] D. Dimitrovski, L. B. Madsen, and T. G. Pedersen, Phys. Rev. B **95**, 035405 (2017).

[39] F. Yang and R.-B. Liu, Phys. Rev. B **90**, 245205 (2014).

[40] E. H. Hwang and S. Das Sarma, Phys. Rev. B **77**, 195412 (2008).

[41] M. Breusing, S. Kuehn, T. Winzer, E. Malić, F. Milde, N. Severin, J. P. Rabe, C. Ropers, A. Knorr, and T. Elsaesser, Phys. Rev. B **83**, 153410 (2011).

[42] E. Malic, T. Winzer, E. Bobkin, and A. Knorr, Phys. Rev. B **84**, 205406 (2011).

[43] D. Brida, A. Tomadin, C. Manzoni, Y. J. Kim, A. Lombardo, S. Milana, R. R. Nair, K. S. Novoselov, A. C. Ferrari, G. Cerullo *et al.*, Nat. Commun. **4**, 1987 (2013).

[44] I. Gierz, J. C. Petersen, M. Mitrano, C. Cacho, I. E. Turcu, E. Springate, A. Stöhr, A. Köhler, U. Starke, and A. Cavalleri, Nat. Mater. **12**, 1119 (2013).

[45] A. Tomadin, D. Brida, G. Cerullo, A. C. Ferrari, and M. Polini, Phys. Rev. B **88**, 035430 (2013).

[46] J. Li, X. Zhang, S. Fu, Y. Feng, B. Hu, and H. Du, Phys. Rev. A **100**, 043404 (2019).

[47] M. Mrudul, Á. Jiménez-Galán, M. Ivanov, and G. Dixit, Optica **8**, 422 (2021).

[48] A. Fleischer, O. Kfir, T. Diskin, P. Sidorenko, and O. Cohen, Nat. Photonics **8**, 543 (2014).

[49] O. Neufeld, D. Podolsky, and O. Cohen, Nat. Commun. **10**, 405 (2019).

[50] T. Huang, L. Li, J. Li, X. Zhu, P. Lan, and P. Lu, J. Physics B: Atomic, Mol. Opt. Phys. **55**, 095601 (2022).